

Interference and switching effect of topological interfacial modes with geometric phase

Xing-Xiang Wang ^{1,2,3,*}, Sho Okada,^{4,*} Towa Maekawa,¹ Liyan Hu,¹ Tomohiro Amemiya ^{1,†} and Xiao Hu ^{5,1,2,3,‡}

¹*School of Engineering, Institute of Science Tokyo, Tokyo 152–8552, Japan*

²*Research Center for Materials Nanoarchitectonics (MANA), National Institute for Materials Science (NIMS), Tsukuba 305-0044, Japan*

³*Graduate School of Science and Technology, University of Tsukuba, Tsukuba 305–8571, Japan*

⁴*Photonic ICT Research Center, National Institute of Information and Communications Technology (NICT), Tokyo 184–8795, Japan*

⁵*Institute for Quantum Science and Technology, Department of Physics, Shanghai University, Shanghai 200444, China*



(Received 2 November 2023; accepted 7 March 2025; published 18 April 2025)

We investigate interference between topological interfacial modes in a semiconductor photonic crystal platform with Dirac frequency dispersions, which can be exploited for interferometry switch. It is demonstrated both theoretically and experimentally that in a two-in/two-out structure with four topological waveguides, geometric phases of the two-component spinor wave functions of topological photonic modes accumulate at turning points of waveguides, which govern the interferences and split the electromagnetic energy into two output ports with relative power ratio tunable by the relative phase of inputs. We show that this photonic phenomenon is intimately related to the spin-momentum locking property of quantum spin Hall effect, and results from the symphonic contributions of three phase variables: the spinor phase and geometric phase upon design, and the global phase controlled from outside. The present findings open the door for manipulating topological interfacial modes, thus exposing a facet of topological physics. The topology-driven interference can be incorporated into other devices and is expected to have far-reaching impacts on advanced photonics, optomechanics, and phononics applications.

DOI: [10.1103/PhysRevResearch.7.023067](https://doi.org/10.1103/PhysRevResearch.7.023067)

I. INTRODUCTION

The information society flourishing nowadays is supported largely by fast data processing based on electronics [1,2] and high-velocity data transfer relying on optics [3]. As is well known, both transport of electrons in integrated circuits (IC) [2] and transformation of signal from electrons to light and vice versa induce heating, which becomes more serious when devices are downsizing and processing speed increases. Light moves faster than electrons and meanwhile does not cause heat, and thus processing information in terms of light is more efficient in principle. Therefore, reducing the times of transformation between optic and electric signals and increasing the usage of light in the stream of information processing are highly desirable. In the growing fields such as artificial intelligence (AI) technology [4,5], the advantage of light data processing is even more obvious [6,7]. The demand on replacing electron by light for information processing would be tremendous in the coming years. However, to harness light is far more difficult than to control electrons, and realizing efficient optic splitter, switch, and isolator is highly desired for advanced data processing based on optic IC.

Photonics topology provides a completely new possibility for controlling light propagation [8–23]. By now topological waveguide propagation robust against disorder, randomness, and sharp corners has been displayed, which breaks the limitation of conventional electromagnetic (EM) wave. As an additional ingredient of topology of bosonic systems, topological interfacial modes have been shown to sustain stable lasing superior to conventional whispering-gallery modes [24–26]. Moreover, wave-function partition of one topological interfacial mode into two topological channels has also been investigated and depends on the mutual angles and/or pseudospin states [27–33]. On the other hand, interference of topological interfacial/edge modes piloted by phases remains largely unexplored so far for both fermionic and bosonic systems.

Here, by studying propagation phenomena of the topological interfacial states along open paths, we explore interference between topological interfacial modes in a semiconductor photonic crystal (PhC) platform. The photonics topology emerges from Kekulé distortions respecting C_{6v} symmetry to honeycomb structure with Dirac frequency dispersions, where gapless helical interfacial modes protected by the mirror and sublattice symmetries appear along the “molecule zigzag” interface between topological PhC and trivial PhC [17,34]. We demonstrate theoretically that in a two-in/two-out structure with four topological waveguides, geometric phases of the two-component spinor wave functions of topological photonic modes accumulate along the designed waveguides, which split the EM energy into two output ports with relative power ratio tunable by the relative phase of inputs. This photonic phenomenon is intimately related to the spin-momentum locking

*These authors contributed equally to this work.

†Contact author: amemiya.t.ab@m.titech.ac.jp

‡Contact author: hu_xiao@shu.edu.cn

Published by the American Physical Society under the terms of the [Creative Commons Attribution 4.0 International](https://creativecommons.org/licenses/by/4.0/) license. Further distribution of this work must maintain attribution to the author(s) and the published article's title, journal citation, and DOI.

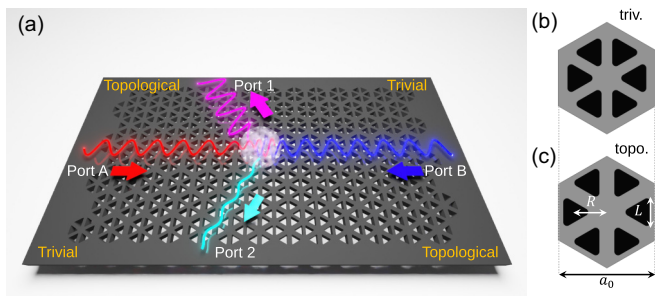


FIG. 1. Schematic of the topological interferometry switch. (a) Photonic crystal (PhC) based on a semiconductor membrane with triangular airholes constituted of two topological domains (upper left and lower right) and two trivial domains (upper right and lower left). The interfaces of the four domains are used as input (ports A and B) and output (ports 1 and 2) ports. Two input waves with a phase difference interfere right on the crossing point of the four topological interfacial waveguides and modulate the ratio of output powers at port 1 and port 2. (b), (c) Structures of unit cells for the trivial and topological PhCs. The lattice constant a_0 and the side length of the triangular airholes L are the same in both structures. R is the distance measured from the center of unit cell to the centers of six airholes. One has $R < a_0/3$ (corresponding to $M > 0$) in a unit cell for the trivial PhC and $R > a_0/3$ (corresponding to $M < 0$) in a unit cell for the topological PhC.

property of quantum spin Hall effect (QSHE), and results from the symphonic contributions of three optic phases: the two-component spinor phase, geometric phase, and global phase, where the first two are upon design and the last one is the handle controllable from outside. We have also performed a proof-of-concept experiment in the communication frequency band based on the Si photonics platform, which is in full agreement with the theoretical analysis. This photonic property is realized due to a unique interplay between the intrinsic bosonic feature of light and the emergent fermionic property encoded in the spin-1/2 spinor wave function in the semiconductor topological waveguide system, which on one hand enables an interferometry switch and on the other hand exposes a facet of topology physics.

II. RESULTS

A. Theoretical analysis and simulations

The frequency dispersion of the honeycomb-type PhC with C_{6v} symmetric Kekulé distortions displayed in Fig. 1(a) is described by the Dirac-type $\mathbf{k} \cdot \mathbf{p}$ Hamiltonian on the basis $\{|p_+\rangle, |d_+\rangle, |p_-\rangle, |d_-\rangle\}$ [13,35],

$$\hat{H} = \begin{bmatrix} -M & -ivk_+ & 0 & 0 \\ ivk_- & M & 0 & 0 \\ 0 & 0 & -M & -ivk_- \\ 0 & 0 & ivk_+ & M \end{bmatrix}, \quad (1)$$

with M the Dirac mass, $v > 0$ the Dirac velocity, and $k_{\pm} = k_x \pm ik_y$, where $\mathbf{k} = (k_x, k_y)$ is measured from the Γ point of the Brillouin zone, and the basis wave functions referring to the field H_z in the hexagonal unit cell for the TE mode. As revealed previously, linear dispersions of topological interface modes persist throughout almost the whole band gap [17];

high-order terms $O(k^2)$ in the $\mathbf{k} \cdot \mathbf{p}$ theory can be neglected as a sufficient approximation, which renders Hamiltonian (1) block diagonalized into the pseudospin-up and -down subspaces (see also Refs. [26,36]). It was shown that the Dirac mass in Eq. (1) takes a positive (negative) value for the trivial (topological) PhC structure with $a_0/R < 3$ ($a_0/R > 3$) as shown in Fig. 1(b) [Fig. 1(c)], characterized by the p - d band inversion [13].

In order to find the functioning principle of the topological interferometry switch, we begin with the topological waveguide mode along a horizontal interface where the topological/trivial PhC occupies the upper/lower half space, respectively, as shown for the input port A in Fig. 1(a) and schematically displayed in Fig. 2(a). For the pseudospin-up sector, one has from Eq. (1)

$$\hat{H}^+ = \begin{bmatrix} -M(y) & -iv\partial_y \\ -iv\partial_y & M(y) \end{bmatrix}, \quad (2)$$

where $k_y = -i\partial_y$ is plugged in, which gives the following solution associated with a zero eigenvalue, i.e., frequency at the center of band gap:

$$\psi(y) = \begin{bmatrix} 1 \\ i \end{bmatrix} e^{yM(y)/v}, \quad (3)$$

where $M(y) = m > 0$ for $y < 0$ and $M(y) = -m < 0$ for $y > 0$ (the Dirac mass is presumed to take the same absolute value m in the two PhCs for simplicity). This is the photonic realization of the Jackiw-Rebbi zero-energy soliton solution originally proposed for fermion number 1/2 field [37]. With the basis taken into account, the full real-space solution of the zero-energy pseudospin-up state is

$$|0, +\rangle = [|p_+\rangle |d_+\rangle] \begin{bmatrix} 1 \\ i \end{bmatrix} e^{yM(y)/v}. \quad (4)$$

Due to the interference between the $|p_+\rangle$ mode and $|d_+\rangle$ mode carrying counterclockwise phase winding with vorticity +1 and +2, respectively [see Figs. 2(b) and 2(c)], there appears a net EM energy flow along the $+x$ direction as displayed in Fig. 2(d), which is consistent with the group velocity of pseudospin-up states [13].

As the time-reversal symmetry counterpart, there is a state supported by the pseudospin-down basis which transports a net EM energy flow along the $-x$ direction. In the setup shown in Fig. 2(a) where the EM signal is injected from the left to the system [corresponding to the input port A in Fig. 1(a)], only the pseudospin-up subspace is relevant due to the spin-momentum locking in the present photonic analog of QSHE. Keep in mind that in topological insulators spin-down electrons go around the outer sample edge and cannot be excluded from the whole interference process, in a sharp contrast to the present photonic system [38–41].

Next, let us consider the EM wave function of the topological interfacial waveguide in the form of an arc between two straight segments: one along the $+x$ direction as discussed above and the other takes an angle θ measured from the x axis [see Fig. 2(a)]. In this case, a polarlike coordinate (θ, ρ) is convenient at the arc segment with radius \mathcal{R} as displayed in

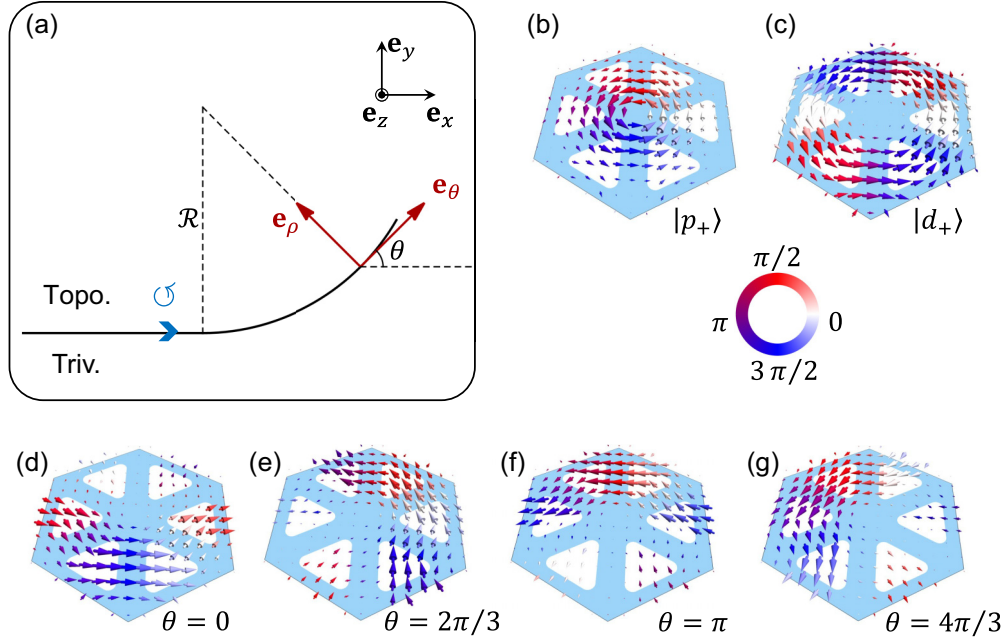


FIG. 2. Transportation of pseudospin-up interfacial modes. (a) Schematic of the polarlike coordinate for a topological interface bent with a fixed radius \mathcal{R} . (b), (c) Pseudospin-up eigenmodes $|p_+\rangle$ and $|d_+\rangle$ at Γ point as the eigen-wave functions in a bulk system, where the arrows represent the local Poynting vectors and the colors of which stand for the phase of wave function. (d)–(g) Pseudospin-up Jackiw-Rebbi modes $|\theta, +\rangle$ with $\theta = 0, \theta = 2\pi/3, \theta = \pi$, and $\theta = 4\pi/3$, respectively, which are obtained by superposing the wave functions of $|p_+\rangle$ and $|d_+\rangle$ in (b) and (c) with relative phase factors associated with the directions of topological interfacial waveguides.

Fig. 2(a) (straight interfaces can be considered formally as the limit $\mathcal{R} \rightarrow \infty$). Here, one has

$$k_{\pm} = k_x \pm ik_y = e^{\pm i\theta}(k_{\theta} \pm ik_{\rho}), \quad (5)$$

with the momentum operators

$$(k_{\theta}, k_{\rho}) = (-i\partial_{\theta}/\mathcal{R}, -i\partial_{\rho}). \quad (6)$$

We separate the pseudospin-up sector of Hamiltonian (1) into two parts:

$$\hat{H}^+ = \begin{bmatrix} -M & -ivk_+ \\ ivk_- & M \end{bmatrix} = \hat{H}_0^+ + \hat{H}_1^+, \quad (7)$$

with

$$\hat{H}_0^+ = \begin{bmatrix} -M & ve^{i\theta}k_{\rho} \\ ve^{-i\theta}k_{\rho} & M \end{bmatrix} = \begin{bmatrix} -M & -ive^{i\theta}\partial_{\rho} \\ -ive^{-i\theta}\partial_{\rho} & M \end{bmatrix} \quad (8)$$

and

$$\hat{H}_1^+ = \begin{bmatrix} 0 & -ive^{i\theta}k_{\theta} \\ ive^{-i\theta}k_{\theta} & 0 \end{bmatrix} = \frac{1}{\mathcal{R}} \begin{bmatrix} 0 & -ve^{i\theta}\partial_{\theta} \\ ve^{-i\theta}\partial_{\theta} & 0 \end{bmatrix}, \quad (9)$$

where \hat{H}_0^+ generates the zero-energy soliton state same as Eq. (2), while \hat{H}_1^+ is responsible for the bending of the interface waveguide which is to be treated as a perturbation [42].

Hamiltonian (8) is solved in the way same as Eq. (2), which yields the zero-energy wave function

$$|\theta, +\rangle = [|p_+\rangle |d_+\rangle] \begin{bmatrix} 1 \\ ie^{-i\theta} \end{bmatrix} F(\rho), \quad (10)$$

with $F(\rho)$ a function taking maximum at the interface ($\rho = 0$) and decaying exponentially into the bulks in the way

shown in Eq. (4). It is obvious that Eq. (10) gives the wave function of the topological interface mode along the straight interface in direction of θ [see Fig. 2(a)]. As can be seen clearly in Figs. 2(e)–2(g) for $\theta = 2\pi/3, \pi$, and $4\pi/3$, respectively, which are compatible with the PhC structure up to the length scale of lattice constant a_0 , the phase factor in the two-component spinor governs the interference between $|p_+\rangle$ mode and $|d_+\rangle$ mode within the unit cell, which yields the net EM energy flow along the interface between the topological and trivial PhCs in the same way as Eq. (4).

Now we treat \hat{H}_1^+ in Eq. (9) by the first-order perturbation, where $|\theta, +\rangle$ in Eq. (10) serves as the unperturbed wave function. Because $e^{i\theta}(-i\partial_{\theta})e^{-i\theta} = -i\partial_{\theta} - 1$, one has

$$\begin{aligned} \tilde{H}_1^+ &= \langle \theta, + | \hat{H}_1^+ | \theta, + \rangle \\ &= \int d\rho F(\rho) [1 - ie^{i\theta}] \begin{bmatrix} 0 & -ive^{i\theta}k_{\parallel} \\ ive^{-i\theta}k_{\parallel} & 0 \end{bmatrix} F(\rho) \begin{bmatrix} 1 \\ ie^{-i\theta} \end{bmatrix} \\ &= \left[v \int d\rho F(\rho)^2 \right] (k_{\parallel} + e^{i\theta}k_{\parallel}e^{-i\theta}) \\ &= \left[\frac{v}{\mathcal{R}} \int d\rho F(\rho)^2 \right] [-i\partial_{\theta} + e^{i\theta}(-i\partial_{\theta})e^{-i\theta}] \\ &= \left[\frac{v}{\mathcal{R}} \int d\rho F(\rho)^2 \right] [-i\partial_{\theta} - i\partial_{\theta} - 1] \\ &= \hbar\omega_0 \left(-i\partial_{\theta} - \frac{1}{2} \right), \end{aligned} \quad (11)$$

with $\hbar\omega_0 = (2v/\mathcal{R}) \int d\rho F(\rho)^2$, where the factor 1/2 in the last result of Eq. (11) appears due to the commutation relation and the Dirac Hamiltonian. Notice that here \hbar is used merely

for the purpose to remind the underlying Dirac physics of the present system, where the dimension of $\hbar\omega_0$ is the inversed area as can be derived from the EM wave equation. One then has the eigenvalue equation for \tilde{H}_1^+ :

$$\hbar\omega_0(-i\partial_\theta - \frac{1}{2})\psi(\theta) = \hbar\omega\psi(\theta), \quad (12)$$

where $\hbar\omega$ is given by $(2\pi f/c)^2$ measured from the band-gap center [13,35], and $\psi(\theta)$ is the coefficient of the unperturbed wave function $|\theta, +\rangle$. For the topological interface waveguide mode at $\omega = 0$ (i.e., the frequency at band-gap center), the solution for Eq. (12) is

$$\psi(\theta) = \psi(\theta_{\text{in}}) \exp[i(\theta - \theta_{\text{in}})/2], \quad (13)$$

with θ_{in} the direction of the topological interface waveguide where the arc segment starts.

Equation (13) indicates that as the Jackiw-Rebbi mode $|\theta, +\rangle$ propagates along an arc segment in the topological interface waveguide, it acquires a phase accumulation corresponding to half of the angle of the arc while the amplitude remains unchanged. Note that at $\omega = 0$, the arc radius \mathcal{R} becomes irrelevant in Eq. (12), which implies that Eq. (13) is applicable to a sharp turn with $\mathcal{R} \sim a_0$ (as will be confirmed by numerical simulations below). It is straightforward to see that Eq. (13) is also applicable to the topological interface waveguide bending to the side of trivial PhC (see Supplemental Material, Note I [43]).

Now we consider the design displayed in Fig. 1(a), where four domains of topological and trivial PhCs form four topological interface waveguides with a crossing point. Owing to the pseudospin-momentum locking associated with the Z_2 topology, the beam from input port A cannot get into the interface channel between the crossing point and the input port B since along this direction of EM flow a pseudospin-down state is required where the topological/trivial PhCs are turned over (namely, the topological/trivial PhCs occupy the lower/upper half space). Therefore, the beam injected from port A is split into the two output channels, port 1 and port 2, with the EM energy equally divided as guaranteed by the device design where the two output channels are mirror symmetric with respect to the input channels [see Fig. 1(a) and Supplemental Material, Fig. S2].

Similarly, the EM wave injected from the input port B propagates along the topological interface waveguide with a pseudospin-up state, which cannot go beyond the crossing point into the interface channel toward input port A, and is split equally in energy into the two output port 1 and port 2. Therefore, as a crucial feature of the present topological interface waveguide system, the two input beams from port A and port B do not form a standing wave in the horizontal interfaces as guaranteed by the pseudospin-momentum locking originated from the Z_2 photonics topology, which is not available in conventional optical waveguide systems.

It is easy to see that the wave function along the straight interface from input port B is also given by Eq. (10) with $\theta = \pi$, and Eq. (13) is also available when the topological interface waveguide is bent (see Supplemental Material, Note I [43]). From Eq. (10) it is clear that the wave functions $|0, +\rangle$ and $|\pi, +\rangle$ are orthogonal to each other [see also Figs. 2(d)

and 2(f)], which corresponds to the pseudospin-momentum locking effect in the above discussions.

In order to verify the above properties, we have checked the branching of the EM beams injected from port A at the crossing point in terms of numerical simulations based on COMSOL [44] (see Appendix A and Supplemental Material, Note II for details). It is seen clearly in Fig. 3(a), where the wave function defined by the out-of-plane magnetic field H_z is displayed for the present TE mode, that the EM beam is split into port 1 and port 2 with approximately equal weights irrespectively of the global phase determined by the chiral source, and it is prevented from propagating beyond the crossing point into the channel toward input port B. Moreover, as displayed in Figs. 3(c)–3(e), one can find that phases along the straight interface segments remain almost constant, since the frequency of chiral source is chosen at the band-gap center which corresponds to a zero Bloch phase upon propagation, in good agreement with theoretical description given in Eq. (10) [see also Eq. (4)]. Noticeably, phase changes are accumulated upon bending into output port 1 and port 2, which take place within a couple of unit cells around the crossing point. These simulation results confirm the theoretical result of Eq. (13). Similarly, one can find the same physics happens when the input port B is excited, as shown in Figs. 3(b) and 3(i)–3(n).

We then proceed to analyze the interference of topological interface modes along the two output channels in the design displayed in Fig. 1(a) when EM waves are injected simultaneously from the input port A and port B. It is clear that the output wave functions are the superpositions of the wave functions contributed by input port A and port B individually. Suppose that the wave functions injected from the two input ports are $e^{i\phi}|0, +\rangle$ at port A and $|\pi, +\rangle$ at port B, where ϕ is the global phase difference between the two input ports which can be controlled from outside, and the output port 1 (port 2) is along the direction of $\theta_1 = 2\pi/3$ ($\theta_2 = 4\pi/3$) as given in Fig. 1(a). According to Eqs. (10) and (13), the output wave functions at the two output ports are given by

$$|1\rangle_{\text{total}} = |1\rangle_{\text{A}} + |1\rangle_{\text{B}} = e^{i(\theta_1 - \pi)/2} [1 + e^{i(\phi + \frac{\pi}{2})}] |\theta_1, +\rangle, \quad (14)$$

and

$$|2\rangle_{\text{total}} = |2\rangle_{\text{A}} + |2\rangle_{\text{B}} = e^{i(\theta_2 - \pi)/2} [1 + e^{i(\phi - \frac{\pi}{2})}] |\theta_2, +\rangle, \quad (15)$$

where the strengths of the two input EM waves are set the same. The output powers at output port 1 and port 2 normalized by the total input power are then evaluated as

$$P_1 = \frac{\langle 1|1\rangle_{\text{total}}}{\langle 1|1\rangle_{\text{total}} + \langle 2|2\rangle_{\text{total}}} = \frac{1}{2}(1 - \sin\phi),$$

$$P_2 = \frac{\langle 2|2\rangle_{\text{total}}}{\langle 1|1\rangle_{\text{total}} + \langle 2|2\rangle_{\text{total}}} = \frac{1}{2}(1 + \sin\phi). \quad (16)$$

Equation (16) shows explicitly that by adjusting the phase difference ϕ between the two input ports, one can continuously manipulate powers at the two output ports, as shown in Fig. 4(a). Especially at $\phi = -\pi/2$, the output is directed totally to port 1 and turned off at port 2, and vice versa at $\phi = \pi/2$. This is the functioning principle of the interferometry switch based on the topological interfacial waveguides.

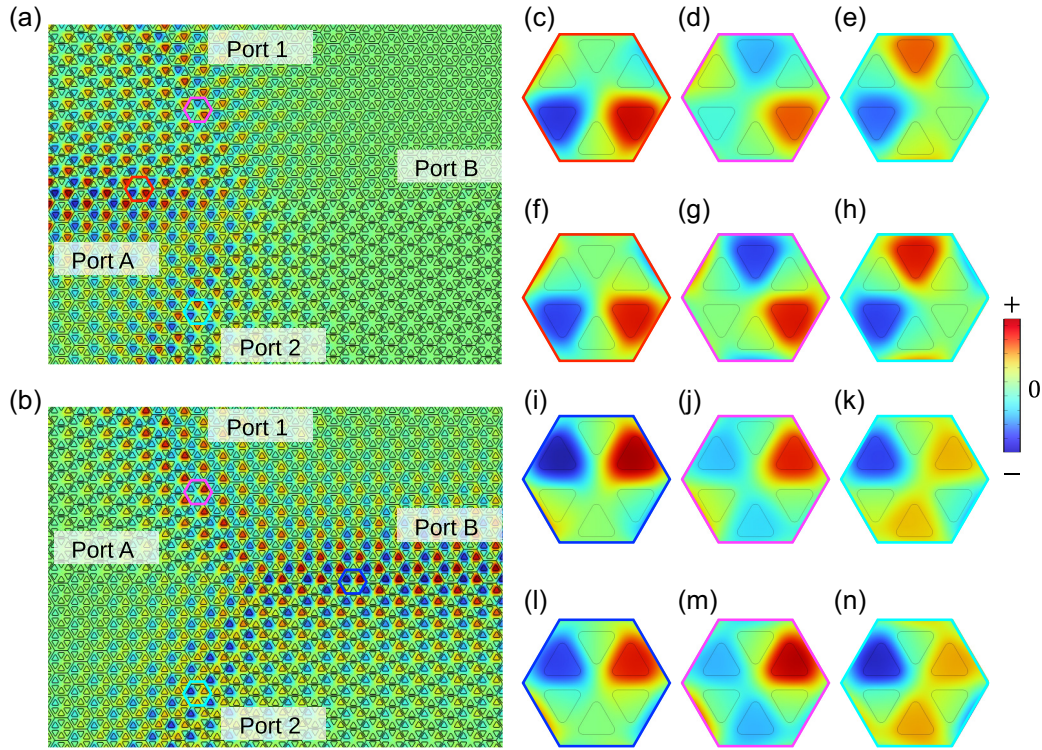


FIG. 3. Splitting of topological interfacial mode obtained by simulations when one of the two input ports is activated. (a) Real part of the simulated wave function H_z (out-of-plane magnetic field), where only port A is activated. (b) Same as (a) except that only port B is activated. (c)–(e) Zoom-in view of wave function inside a typical unit cell encompassed by color hexagon at port A, port 1, and port 2, respectively, in (a). The corresponding unit cells in (a) and (c)–(e) are marked by hexagonal frames with the same colors. (f)–(h) Wave functions constructed by superposing $|p_+\rangle$ and $|d_+\rangle$ using the expressions of $|A\rangle$, $|1\rangle_A$, and $|2\rangle_A$ obtained theoretically according to Eqs. (10) and (13) (see also Supplemental Material, Note III [43]), which match well with those in (c)–(e). (i)–(n) Same as (c)–(h) except that only port B is activated. Color looks different for the real parts of wave functions in (a) and (b) due to different phase accumulations while the whole intensity of EM wave is the same.

One can also rewrite Eqs. (14) and (15) into a scattering matrix (S-matrix):

$$S = \frac{1}{\sqrt{2}} \begin{bmatrix} e^{i\frac{\theta_1}{2}} & -ie^{i\frac{\theta_1}{2}} \\ -e^{i\frac{\theta_2}{2}} & -ie^{i\frac{\theta_2}{2}} \end{bmatrix} = \frac{1}{\sqrt{2}} \begin{bmatrix} e^{i\frac{\theta_1-\pi}{2}} & 0 \\ 0 & e^{i\frac{\theta_2-\pi}{2}} \end{bmatrix} \begin{bmatrix} e^{i\frac{\pi}{2}} & 1 \\ e^{-i\frac{\pi}{2}} & 1 \end{bmatrix}, \quad (17)$$

with $\psi_{\text{out}} = S\psi_{\text{in}}$, where the input wave function is $\psi_{\text{in}} = [e^{i\phi} \ 1]^T / \sqrt{2}$ on the basis $\{|0, +\rangle, |\pi, +\rangle\}$ and the output wave function is on the basis $\{|\theta_1, +\rangle, |\theta_2, +\rangle\}$. Note that the S-matrix (17) is unitary, which satisfies the energy conservation. In general, the S-matrix is 4×4 for a 2-in/2-out system. Here, the S-matrix is reduced to 2×2 due to the suppression of backscattering in the topological interfacial modes. With a 2×2 unitary S-matrix one can derive a sinusoidal power distribution with a phase shift, which depends on system details and in many cases cannot be given explicitly. In the present work, the phase given by Eq. (13) of a topological interfacial mode upon bending uniquely determines elements of the S-matrix and consequently the phase shift.

The switching effect can also be confirmed by numerical simulations, where the input port A and port B are simultaneously stimulated and the relative phase between the two inputs

is tuned. Figure 4(a) clearly illustrates that powers at output port 1 and port 2 exhibit a sinusoidal variation upon tuning ϕ , which is in excellent agreement with Eq. (16) derived from theoretical analysis. We display in Figs. 4(b)–4(f) the distribution of intensity of the EM wave in terms of $|H_z|^2$ at several values of ϕ to visualize the switching process. At $\phi = -\pi/2$, the output is almost entirely directed to port 1. As ϕ increases to $\phi = -\pi/4$, there is a slight transfer of power to output port 2. At $\phi = 0$, the two output ports exhibit nearly equal powers. When $\phi = \pi/4$, the output is primarily directed to port 2. Finally, at $\phi = \pi/2$, the output power at port 1 is suppressed almost completely. The whole switching process occurs due to the interference of the wave functions contributed by port A and port B (see Supplemental Material, Note IV [43] for comprehensive simulation results), as indicated in the theoretical discussions.

It is worth noticing that the nontrivial phase accumulation encoded in the factor of $1/2$ in Eq. (13) upon bending of the topological interface waveguide along an arc is crucial for the switching effect given in Eq. (16). As seen in Eqs. (14) and (15), the relative direction change of beams injected from input port A and port B is of π for the EM wave function in output port 1, and of $-\pi$ for output port 2. The reason why they can generate EM energy flows different in the two output ports is that the phase accumulations induced by the direction

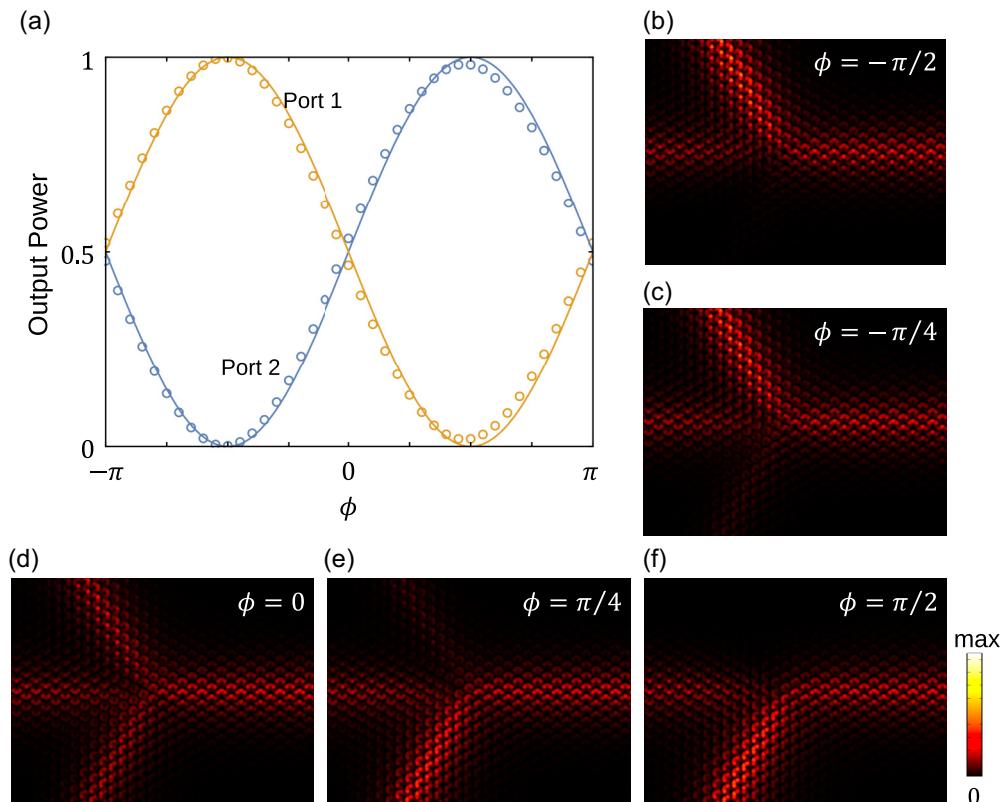


FIG. 4. Interferometry switching phenomena when two input ports are activated simultaneously with finite phase difference. (a) Proportion of the total output power at port 1 (yellow) and port 2 (blue) as function of the phase difference ϕ between input port B and port A. Circle marks are for simulated results, whereas the solid lines are for the theoretical results given by Eq. (16). (b)–(f) Simulated distribution of the field strength $|H_z|^2$ for $\phi = -\pi/2$, $\phi = -\pi/4$, $\phi = 0$, $\phi = \pi/4$, and $\phi = \pi/2$, respectively.

changes yield phase factors $e^{i\pi/2}$ and $e^{-i\pi/2}$ unequal to each other in the last equality in Eqs. (14) and (15) (without the factor 1/2, one would have $e^{i\pi} = e^{-i\pi}$).

Although the discussions so far focus on frequency at the band-gap center (namely $\omega = 0$), we notice that the switching effect remains intact for $\omega \neq 0$ in the present design with sharp bending in topological waveguides at the crossing point which ensures $|\omega|/\omega_0 \ll 1$ for frequency in the band gap. As a matter of fact, we show explicitly by COMSOL simulations that using $\omega \neq 0$ only slides the switching curve along the axis of phase difference (see Supplemental Material, Note IX [43]), which can be understood as the Bloch phases piled up during propagation along the topological waveguides. This observation indicates that in the present design the topological interference and switching effect is available for frequency in the whole bulk band gap, a topological protection.

In short, by both theory and COMSOL simulations, we show that the phase of the topological interface mode with given pseudospin changes at a bent interface, namely in a one-in/one-out structure, by the amount equal to half of the angle subtended by the arc. With a branching present, namely in the one-in/two-out structure, the phase changes upon branching are in accordance with that derived based on the one-in/one-out structure, while the EM energy is split equally into two output ports due to the mirror symmetric arrangement in the present device. It is noticed that with only one input, no dynamical switching effect can be expected. We then

demonstrate that using the two-in/two-out structure and tuning the phase difference between the two inputs, one can achieve a complete switching. The topological switching effect is available in the whole band gap.

B. Experimental demonstration of the switching effect

We perform a proof-of-concept experiment based on silicon photonics, which is considered as a significant platform for optical applications due to its transparency in the optical communication band and the fabricability via modern semiconductor manufacturing technologies [45].

First we fabricated the sample on a silicon-on-insulator (SOI) wafer, with a c-Si/SiO₂/Si layer structure from bottom to top in the vertical direction. The thickness of the c-Si substrate is 525 μm , while the thicknesses of the SiO₂ BOX layer and Si active layer above it are 1.5 μm and 220 nm, respectively. Using electron-beam (EB) lithography and dry-etching techniques, we patterned the Si layer as design. Subsequently, a 1- μm -thick SiO₂ layer was deposited on top of the silicon membrane using the plasma chemical vapor deposition (PCVD) method (see Appendix B and Supplemental Material, Note VI [43] for further details on the fabrication process). Because the dielectric permittivity of silicon is much larger than SiO₂, the EM wave is well confined within the silicon membrane region, and thus the resultant structure of the PhC can be considered as a silicon membrane cladded by

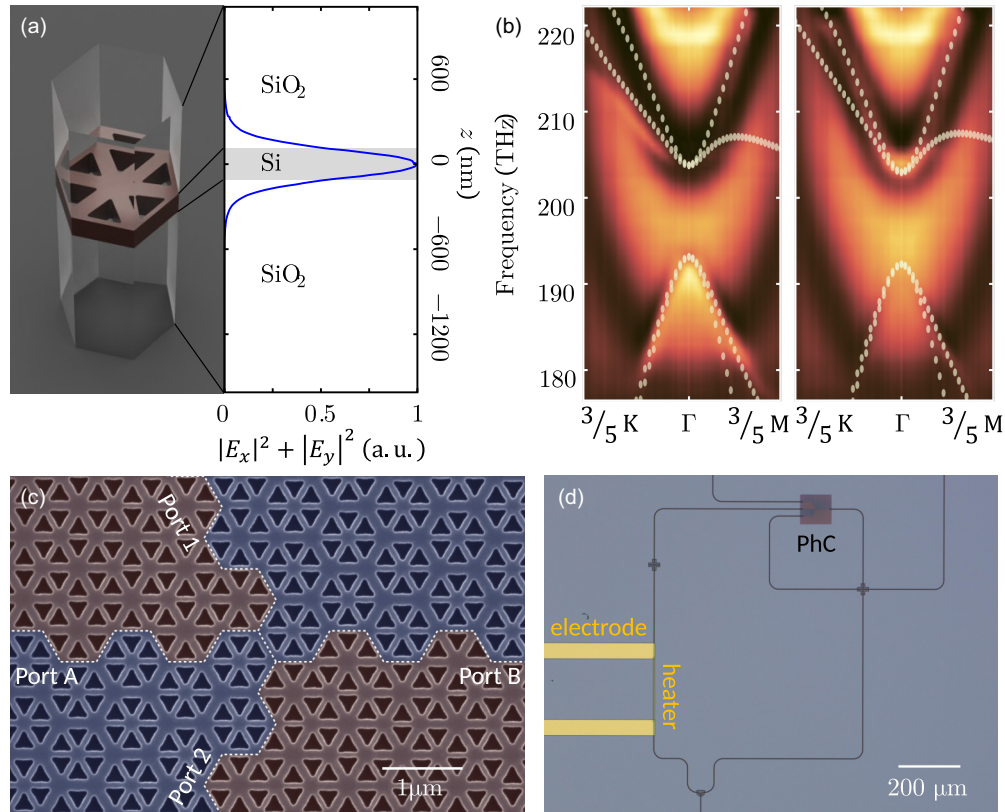


FIG. 5. Fabricated sample. (a) Schematic plot of the $\text{SiO}_2/\text{Si}/\text{SiO}_2$ cladding structure. The right panel is the simulated distribution of the electric field intensity for TE modes. (b) Measured band structure of the fabricated sample. Left and right panels are for trivial and topological PhCs, respectively. Dotted lines are 3D simulation results for the structure shown in the left panel of (a). (c) SEM image for the central region of the fabricated PhC. Color shadings and white dashed lines are added as visual guides for the trivial (blue) and topological (red) regions, as well as their interfaces. (d) Overall look for the experimentally fabricated sample taken by the optical microscope.

SiO_2 layers, as illustrated schematically in Fig. 5(a). In order to confirm the function of this structure, we performed a three-dimensional finite-element simulation for the cladding structure based on COMSOL. The intensity distribution of the electric field along the vertical direction is plotted in the right panel of Fig. 5(a), where the field intensity decays rapidly in the SiO_2 layer and almost vanishes within a thickness of 500 nm. The simulated bulk band dispersion based on COMSOL agrees well with the measured band structure, as shown in Fig. 5(b). The band-gap center is estimated to be $\lambda = 1521$ nm based on the wavelength of the band edge, and this value is used as the wavelength of the input light source during the measurement procedure. Figure 5(c) shows a scanning electron microscope (SEM) image of the central part of the fabricated PhC, with colors and white dashed lines indicating topologically distinct regions and their interfaces, where interference of topological interfacial modes and the switching effect are expected to happen.

In addition to the PhC structure for the topological switching effect, we also fabricated silicon waveguides which couple to the ports of the PhC. As shown in Fig. 5(d), the silicon waveguides connected to the two input ports of the PhC are split from a common silicon waveguide by a Y-splitter (see the bottom part), and these two waveguides are designed with equal length, which ensures an equal phase of the EM wave at the two input ports of PhC before tuning. In order to

control the phase difference between the inputs for showing the switching effect discussed theoretically, we fabricated an electric heater on the top of one input waveguide using optical maskless lithography and EB evaporation (see Appendix B and Supplemental Material, Note VI for details [43]), as depicted in Fig. 5(d). When electric current flows through the heater, the temperature of the waveguide beneath increases, which results in the change of the refractive index of the waveguide and a phase shift of the corresponding input EM wave. In the present experiment, the ambient temperature is set as room temperature, and the wavelength of the input source is fixed at 1521 nm (the band-gap center of the PhC). Under this condition, the refractive index of the silicon waveguide is a linear function of temperature change [46], which is proportional to the power provided by the electric current. Because the length of the heater is fixed, the phase shift induced by the heater should also be a linear function of the electric power.

Therefore, the switching effect discussed theoretically can be examined experimentally by checking the output powers from PhC as a function of the electric power P applied to the heater. In Fig. 6(a), the circles represent the measured power ratio at the two output ports, while the dashed sinusoidal curves indicate the switching curve expected from theory. Overall, the experimental results are in full agreement with the theoretical curve, and the maximum output power at one

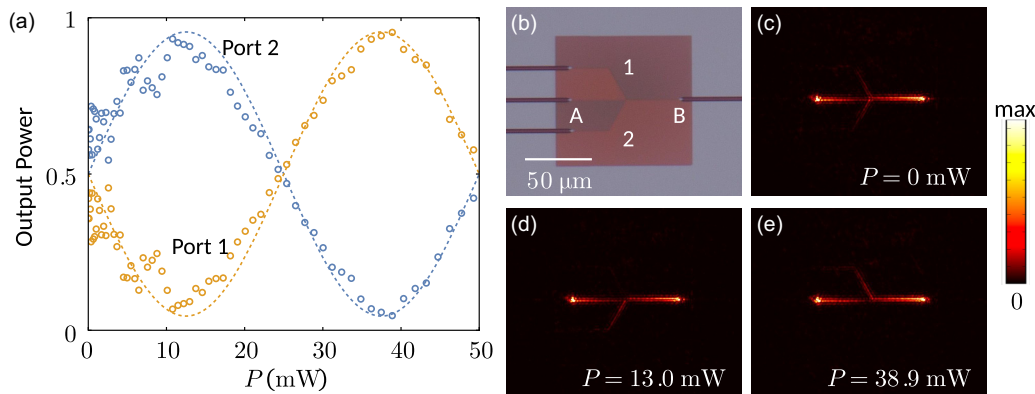


FIG. 6. Experimentally measured interferometry switching phenomena. (a) Proportion of the output power at port 1 (yellow) and port 2 (blue) as function of the electric power P applied to the heater displayed in Fig. 5(d). Circle marks are measured results, whereas the dashed lines stand for the sinusoidal curve expected from the theoretical analysis. (b) Zoomed-in optical microscope image of the PhC. (c)–(e) Photos taken by infrared camera for the region shown in b, with $P = 0$ mW, $P = 13.0$ mW, and $P = 38.9$ mW, respectively.

output port is 10 dB higher than the minimum power at the other. Figures 6(c)–6(e) show the scattered light taken by an infrared camera set above the sample at three typical values of the electric power P . At $P = 0$ mW, with no current flowing through the heater, the phases at the two input ports are the same, resulting in identical field intensities at the two output ports. As the voltage across the heater increases, at $P = 13.0$ mW and $P = 38.9$ mW, the switching effect occurs, and the EM wave is directed almost exclusively to output ports 1 and 2, respectively. In Fig. 6(a), data points are more scattered at low electric powers than at high electric powers, which can be understood as follows: in the present experiment, phase difference is controlled by heating the waveguide which is exposed to air; at low electric powers, the difference between the waveguide temperature and room temperature is small, making it more susceptible to fluctuations of room temperature.

III. DISCUSSION

A. Geometric phase

The switching effect addressed above has a clear underlying physics of geometric phase [47,48] associated with the Dirac Hamiltonian. Considering the basis wave function $|\theta, +\rangle = [1 \quad ie^{-i\theta}]^T / \sqrt{2}$ in Eq. (10), which adiabatically evolves in the one-dimensional parametric space θ , the geometric phase accumulated in the waveguide bent from θ_{in} to θ is evaluated as [47,48]

$$\gamma(\theta_{\text{in}}, \theta) = \int_{\theta_{\text{in}}}^{\theta} d\theta \langle \theta, + | i\partial_{\theta} | \theta, + \rangle = \frac{1}{2} \int_{\theta_{\text{in}}}^{\theta} d\theta = (\theta - \theta_{\text{in}})/2, \quad (18)$$

which gives directly Eq. (13). While the above result is gauge dependent since the path is not closed, it is clear that the relation Eq. (13) for $\psi(\theta)$ is gauge independent since it refers to the measurable physical quantity (see Supplemental Material, Note VII). During the derivation of Eq. (13), we perceive the interface bending as a perturbation, and require the wave function to stay at zero energy under this perturbation. This treatment corresponds to the above adiabatic evolution without altering the energy level of the eigenstate. Therefore, the

explicit derivations based on the $\mathbf{k} \cdot \mathbf{p}$ theory reveal successfully an aspect of geometric phase, and these two viewpoints together provide a comprehensive picture for the topological interference and switching effect.

B. Spin-1/2 degree of freedom

The phenomena discussed above can also be captured in terms of spin-1/2 degree of freedom of the topological interface mode. The block-diagonalized Dirac Hamiltonian (1) governs the two-component spinor on basis $\{|p_+\rangle, |d_+\rangle\}$ characterized by a fermionic field with $s = 1/2$ [37]. From Eq. (10), one has $\langle \sigma_x \rangle = \sin \theta$ and $\langle \sigma_y \rangle = \cos \theta$, and the EM beam injected from input port A and port B corresponds to state $\langle \sigma_y \rangle = 1$ and $\langle \sigma_y \rangle = -1$, respectively ($\langle \sigma_x \rangle = 0$ in both cases). Upon conflating into output port 1 (port 2) the spin rotates by $\delta\theta = \pi$ ($-\pi$) and induces relative phase factor $e^{is\delta\theta} = e^{i\pi/2}$ ($e^{-i\pi/2}$), which contributes to Eqs. (14) and (15) with opposite signs. On the other hand, the injection of EM beams from the input port A and port B toward the crossing point of topological interfacial waveguides is certainly inherited from the Bose-Einstein statistics of photons, which induces interferences along the output channels. Therefore, the topological switching effect uncovered in the present work is due to the unique interplay between the intrinsic bosonic feature of light and the emergent fermionic property encoded in the spin-1/2 spinor wave function in the semiconductor topological waveguide system.

C. Zero-energy mode

In the present work, we adopt the design based on the so-called “molecule zigzag” interface (see Supplemental Material, Note II), where the existence of the zero-energy topological interfacial mode is guaranteed by the mirror symmetry and chiral (i.e., sublattice) symmetry [34] (see also experiments in Ref. [17]). We have also confirmed that all the results presented here remain valid in a design based on the “arm-chair” interface (see Supplemental Material, Note V), where the tiny minigap in dispersions of topological interfacial modes due to the weak crystalline symmetry breaking at interfaces [13] is naturally smeared out by the finite system size in simulations as well as in practical devices.

D. Possible quick switching

Generally speaking, ω/ω_0 is not necessarily a small number as in systems with a large band gap and absence of sharp bends in topological waveguides. It is easy to see that the switching effect disappears when frequency matches the condition $|\omega|/\omega_0 = l + 1/2$ with integer l . Surprisingly, we find that a complete switching requires only a small phase difference ϕ between the two inputs when frequency gets close to this discrete set of normalized values (see Supplemental Material, Note X [43]). This intriguing behavior originating from Dirac physics hints that response time of optic switches (and their sizes) may be reduced drastically, which is extremely useful in photonics devices.

E. Previous designs for beam splitting and switching

Wave-function partition, or beam splitting, of topological interfacial modes has been addressed in previous works [27–33], which is shown to depend on the mutual angles between one input port and two output ports. In stark contrast, in the present work we design the topological waveguide system in such a way that the two output ports are symmetric with respect to the input ports, which guarantees the equal energy partition when only one input port is fed. The topological switch effect toward two output ports is purely due to the interference between the two topological input beams, which is piloted by the relative phase difference of the two input ports.

Recently, proposals on photonic switching associated with topological effects have appeared. One approach is to apply external magnetic field, which alters the bulk band structure with the time-reversal symmetry breaking [49,50]. While the topological modes are stable as protected by the Chern number, the switching process will be slow associated with the onset of external magnetic field to the whole sample. Because of the use of gyrotropic effect, the switching effect simply fades away when frequency is lifted to telecommunication frequency where the main photonics applications focus. The other approaches use valley photonics or Floquet physics [51,52], where the switching is achieved by manipulating the polarization of input wave function, which is quite different from the present work. In stark contrast, our system is fully based on dielectrics without external magnetic field that can be controlled in terms of silicon waveguides, and the switching effect is purely optic and linear.

F. Robustness to randomness

The results of the proof-of-concept experiment are in full agreement with the theoretical analysis. In order to examine the robustness of the topological switching effect we also performed COMSOL simulations with random deformations in PhCs, such as shifts in positions and changes in size of triangle air holes in the dielectric slab, with the standard variations larger than the roughness of modern fabrication technology [19,53]. With the presence of such randomness, the sinusoidal form of the topological interference curve remained intact. This observation indicates another aspect of topological protection of the present switching effect.

G. Device applications

The key interferences of topological interfacial modes take place around the crossing point within several unit cells, with the length scale of $\sim 3 \mu\text{m}$ at the telecommunication frequency, which sets the limiting device size of the present topological switch [see simulation results in Figs. 4(a) and 4(b)]. This structure may also be incorporated into other Mach-Zehnder-type devices [54].

The present topological switch can be easily implanted into silicon nanophotonic systems, since it has been demonstrated experimentally that the conventional silicon waveguides with simple TE/TM modes can be smoothly converted into the topological interfacial waveguides and vice versa [53], which therefore can work as the low-loss input and output ports for the present topological interferometry switch. The optical switching effect addressed in the present study can work as a building block for other key elements of light IC, such as diode and transistors [1].

The interference and switching functions of the topological interfacial waveguide modes shown in the present work are available for other wave systems with intrinsic bosonic feature, including optomechanical, surface acoustic, and phononic waves [22,55,56]. Applications of the basic idea of the present approach to electronic systems, such as exciton-polariton structures, are also anticipated [20]. All these are expected to boost discontinuous leaps in exploiting matter topology for new phenomena and innovative technologies.

ACKNOWLEDGMENTS

This work was partially supported by CREST, JST (Core Research for Evolutionary Science and Technology, Japan Science and Technology Agency) (Grant No. JP-MJCR18T4), Grant No. JPJSBP-120219942 and the Shanghai Science and Technology Innovation Action Plan (Grant No. 24LZ1400800) (X.H.), and partially supported by ASPIRE, JST (Adopting Sustainable Partnerships for Innovative Research Ecosystem, Japan Science and Technology Agency) (Grant No. 23837157) (T.A.). We are grateful to M. Kawasaki for stimulating discussions.

X.H. and T.A. conceived and supervised the project; X-X.W. and X.H. performed the analytical calculations and wrote the manuscript; X-X.W. performed the computer simulations; T.A. guided the experimental process; X-X.W. and S.O. fabricated the sample and conducted the experimental measurements; and T.M. and L.H. provided assistance in the experiments. All authors fully contributed to the research.

The authors declare no competing financial and nonfinancial interests.

DATA AVAILABILITY

All the codes that support the findings of this study are available from the corresponding authors upon reasonable request, following the policy of JST.

APPENDIX A: NUMERICAL SIMULATIONS

All the numerical simulations presented in this study were performed using the finite-element method implemented in

COMSOL MULTIPHYSICS software [44]. The topological PhC platform in the present work was considered as a dielectric slab with hexagonal unit cells, each containing six airhole and respecting C_{6v} symmetry (see Fig. 1 in the main text). In order to reduce computation resource, we emulated the topological waveguide switch device by considering physical parameters and EM fields uniform in the z direction, which transfers numerical calculations into purely 2D in the theoretical part. For a silicon slab with thickness ~ 200 nm, the relative permittivity was taken as $\epsilon_r = 7$. The lattice constant of the PhC was $a_0 = 800$ nm, with each hexagonal unit cell containing six triangular airholes, and the side length of each airhole was $L = 270$ nm. In the case of the trivial PhC, the distance from the center of unit cell to the center of airholes was $R = 245$ nm ($< a_0/3$), while for the topological PhC, this distance was $R = 280$ nm ($> a_0/3$). The total topological switch in the simulations (see Figs. 3 and 4) consisted of 47 unit cells along the longer side and 24 unit cells along the shorter side, and was separated into four regions by the interfaces between the topological and trivial domains (see also Supplemental Material, Note II [43]). A chiral source was placed at the center of a unit cell at the end of each input port, formed by a cluster of six pointlike sources arranged in the shape of a small hexagon with a 2π phase winding (a phase difference of $\pi/3$ between neighboring point sources) in the counterclockwise direction, which induced the pseudospin-up topological interfacial modes in the system.

We also performed 3D simulations for the $\text{SiO}_2/\text{Si}/\text{SiO}_2$ cladding structure presented in Figs. 5(a) and 5(b), where the lattice constant and airhole size were kept the same as in the 2D simulations, while the thickness of the layers from bottom to top was 1.5 μm , 220 nm, and 1 μm , respectively. The relative permittivity of Si and SiO_2 was taken as $\epsilon_r = 11.7$ and $\epsilon_r = 2.088$, respectively. Since in the PCVD process SiO_2 could not fill up the airholes in the Si layer, the permittivity of the airholes was set as $\epsilon_r = 1$. A perfectly matched layer was adopted at the top and bottom surface.

APPENDIX B: SAMPLE FABRICATION

The SOI wafer used in this work was produced by SEIREN KST Corp., with the thicknesses of the c-Si substrate, SiO_2

BOX layer, and Si active layer being 525 μm , 1.5 μm , and 220 nm, respectively. The wafer was first cleaned using the following sequence: acetone boiling (3 min), methanol (2 min), acetone boiling (3 min), methanol (2 min), running water (2 min), sulfuric acid (3 min), running water (2 min), 7% buffered hydrofluoric acid (BHF) (30 s), and finally running water (3 min).

EB lithography was performed (see also Supplemental Material, Note VI [43]) to pattern the PhC (geometric size same as the 2D numerical simulations) and the waveguide (width of 700 nm) design on a positive resist ZEP-520A (maker: ZEON Corp.) spin coated onto the wafer, with the thickness of 500 nm. Subsequently, the resist was developed in ZED-N50 (maker: ZEON Corp.) for 60 s, followed by cleaning with isopropyl alcohol (30 s, twice) to remove the developing solution. The dry etching using CF_4/SF_6 mixture gas was applied to transfer the designed pattern into the Si active layer (see also Supplemental Material, Note VI). Dimethylacetamide (DMAc) (60 $^\circ\text{C}$, 24 h) was used to remove the rest of the resist, followed by the cleaning process using acetone boiling (3 min), methanol (2 min), and running water (3 min). Plasma chemical vapor deposition (PCVD) was processed to deposit a 1- μm -thick SiO_2 layer above the wafer (see also Supplemental Material, Note VI).

In order to pattern the heater above the silicon waveguide, hexamethyldisilazane (OAP) and two types of positive resist (PMGI SF-9 and AZ5200NJ) were spin coated on top of the SiO_2 layer (see also Supplemental Material, Note VI). The heater region was then exposed to 375-nm ultraviolet light using optical maskless lithography (model: DNK MX-1205, exposure speed: 3.6 mm/s, LD intensity: 90%). After development of the resist with AZ300MIF for 105 s, the resist in the exposed region was removed. EB evaporation was then conducted to deposit a 50-nm-thick titanium layer onto the uncovered surface of SiO_2 as the electric heater, followed by a 5-nm layer of gold to prevent oxidation of the titanium. A lift-off processed by acetone boiling for 2 h was performed to remove the remaining resist along with the metal deposited on top of it, followed by cleaning up using methanol (3 min) and running water (1 min). Subsequently, the electrode part was fabricated using the same process as the heater, except that the thickness of the gold layer was 500 nm.

-
- [1] H. R. Huff, John Bardeen and transistor physics, *AIP Conf. Proc.* **550**, 3 (2001).
 - [2] P. Horowitz and W. Hill, *The Art of Electronics* (Cambridge University Press, Cambridge, 1989).
 - [3] C. K. Kao, *Optical Fiber Technology II: Vol. 2* (IEEE, New York, 1981).
 - [4] S. J. Russell and P. Norvig, *Artificial Intelligence: A Modern Approach* (Pearson, Hoboken, 2021).
 - [5] E. Rich and K. Knight, *Artificial Intelligence*, 3rd ed. (McGraw-Hill-India, New Delhi, 2010).
 - [6] Y. Shen, N. C. Harris, S. Skirlo, M. Prabhu, T. Baehr-Jones, M. Hochberg, X. Sun, S. Zhao, H. Larochelle, D. Englund, and M. Soljačić, Deep learning with coherent nanophotonic circuits, *Nat. Photonics* **11**, 441 (2017).
 - [7] Z. Chen, A. Sludds, R. Davis, I. Christen, L. Bernstein, L. Ateshian, T. Heuser, N. Heermeier, J. A. Lott, S. Reitzenstein, R. Hamerly, and D. Englund, Deep learning with coherent VCSEL neural networks, *Nat. Photonics* **17**, 723 (2023).
 - [8] F. D. M. Haldane and S. Raghu, Possible realization of directional optical waveguides in photonic crystals with broken time-reversal symmetry, *Phys. Rev. Lett.* **100**, 013904 (2008).
 - [9] Z. Wang, Y. Chong, J. D. Joannopoulos, and M. Soljačić, Observation of unidirectional backscattering-immune topological electromagnetic states, *Nature (London)* **461**, 772 (2009).
 - [10] M. Hafezi, S. Mittal, J. Fan, A. Migdall, and J. M. Taylor, Imaging topological edge states in silicon photonics, *Nat. Photonics* **7**, 1001 (2013).

- [11] M. C. Rechtsman, J. M. Zeuner, Y. Plotnik, Y. Lumer, D. Podolsky, F. Dreisow, S. Nolte, M. Segev, and A. Szameit, Photonic Floquet topological insulators, *Nature (London)* **496**, 196 (2013).
- [12] A. B. Khanikaev, S. H. Mousavi, W.-K. Tse, M. Kargarian, A. H. MacDonald, and G. Shvets, Photonic topological insulators, *Nat. Mater.* **12**, 233 (2013).
- [13] L.-H. Wu and X. Hu, Scheme for achieving a topological photonic crystal by using dielectric material, *Phys. Rev. Lett.* **114**, 223901 (2015).
- [14] T. Ozawa, H. M. Price, A. Amo, N. Goldman, M. Hafezi, L. Lu, M. C. Rechtsman, D. Schuster, J. Simon, O. Zilberberg, and I. Carusotto, Topological photonics., *Rev. Mod. Phys.* **91**, 015006 (2019).
- [15] Y. Yang, Y. F. Xu, T. Xu, H.-X. Wang, J.-H. Jiang, X. Hu, and Z. H. Hang, Visualization of a unidirectional electromagnetic waveguide using topological photonic crystals made of dielectric materials, *Phys. Rev. Lett.* **120**, 217401 (2018).
- [16] S. Barik, A. Karasahin, C. Flower, T. Cai, H. Miyake, W. DeGottardi, M. Hafezi, and E. Waks, A topological quantum optics interface, *Science* **359**, 666 (2018).
- [17] N. Parappurath, F. Alpeggiani, L. Kuipers, and E. Verhagen, Direct observation of topological edge states in silicon photonic crystals: Spin, dispersion, and chiral routing, *Sci. Adv.* **6**, eaaw4137 (2020).
- [18] Z. K. Shao, H. Z. Chen, S. Wang, X. R. Mao, Z. Q. Yang, S. L. Wang, X.-X. Wang, X. Hu, and R. M. Ma, A high-performance topological bulk laser based on band-inversion-induced reflection, *Nat. Nanotechnol.* **15**, 67 (2020).
- [19] H. Kagami, T. Amemiya, S. Okada, N. Nishiyama, and X. Hu, Highly efficient vertical coupling to a topological waveguide with defect structure, *Opt. Express* **29**, 32755 (2021).
- [20] W. Liu, Z. Ji, Y. Wang, G. Modi, M. Hwang, B. Zheng, V. J. Sorger, A. Pan, and R. Agarwal, Generation of helical topological exciton-polaritons, *Science* **370**, 600 (2020).
- [21] Z. Yang, E. Lustig, G. Harari, Y. Plotnik., Y. Lumer, M. A. Bandres, and M. Segev, Mode-locked topological insulator laser utilizing synthetic dimensions, *Phys. Rev. X* **10**, 011059 (2020).
- [22] S. Guddala, F. Komissarenko, S. Kiriushechkina, A. Vakulenko, M. Li, V. M. Menon, A. Alù, and A. B. Khanikaev, Topological phonon-polariton funneling in midinfrared, *Science* **374**, 225 (2021).
- [23] V. Peano, F. Sapper, and F. Marquardt, Rapid exploration of topological band structures using deep learning, *Phys. Rev. X* **11**, 021052 (2021).
- [24] A. Dikopoltsev, T. H. Harder, E. Lustig, O. A. Egorov, J. Beierlein, A. Wolf, Y. Lumer, M. Emmerling, C. Schneider, S. Höfling, M. Segev, and S. Klembt, Topological insulator vertical-cavity laser array, *Science* **373**, 1514 (2021).
- [25] X.-C. Sun, X.-X. Wang, T. Amemiya, and X. Hu, Comment on “Spin-momentum-locked edge mode for topological vortex lasing,” *Phys. Rev. Lett.* **127**, 209401 (2021).
- [26] X.-C. Sun and X. Hu, Topological ring-cavity laser formed by honeycomb photonic crystals, *Phys. Rev. B* **103**, 245305 (2021).
- [27] X. Cheng, C. Jouvaud, X. Ni, S. H. Mousavi, A. Z. Genack, and A. B. Khanikaev, Robust reconfigurable electromagnetic pathways within a photonic topological insulator, *Nat. Mater.* **15**, 542 (2016).
- [28] Z. Qiao, J. Jung, C. Lin, Y. Ren, A. H. MacDonald, and Q. Niu, Current partition at topological channel intersections, *Phys. Rev. Lett.* **112**, 206601 (2014).
- [29] M. Yan, J. Lu, F. Li, W. Deng, X. Huang, J. Ma, and Z. Liu, On-chip valley topological materials for elastic wave manipulation, *Nat. Mater.* **17**, 993 (2018).
- [30] X. Wu, Y. Meng, J. Tian, Y. Huang, H. Xiang, D. Han, and W. Wen, Direct observation of valley-polarized topological edge states in designer surface plasmon crystals, *Nat. Commun.* **8**, 1304 (2017).
- [31] L. Zhang, Y. Yang, M. He, H. Wang, Z. Yang, E. Li, F. Gao, B. Zhang, R. Singh, J. Jiang, and H. Chen, Valley kink states and topological channel intersections in substrate-integrated photonic circuitry, *Laser Photon. Rev.* **13**, 1900159 (2019).
- [32] Y. Kang, X. Ni, X. Cheng, A. B. Khanikaev, and A. Z. Genack, Pseudo-spin-valley coupled edge states in a photonic topological insulator, *Nat. Commun.* **9**, 3029 (2018).
- [33] Y. Yang, X. Qian, Li. Shi, X. Shen, and Z. Hang, Unidirectional transport in amorphous topological photonic crystals, *Sci. China Phys. Mech. Astron.* **66**, 274212 (2023).
- [34] T. Kariyado and X. Hu, Topological states characterized by mirror winding numbers in graphene with bond modulation, *Sci. Rep.* **7**, 16515 (2017).
- [35] S. Barik, H. Miyake, W. DeGottardi, E. Waks, and M. Hafezi, Two-dimensionally confined topological edge states in photonic crystals, *New J. Phys.* **18**, 113013 (2016).
- [36] X.-X. Wang, Z. Guo, J. Song, H. Jiang, H. Chen, and X. Hu, Unique Huygens-Fresnel electromagnetic transportation of chiral Dirac wavelet in topological photonic crystal, *Nat. Commun.* **14**, 3040 (2023).
- [37] R. Jackiw and C. Rebbi, Solitons with fermion number $\frac{1}{2}$, *Phys. Rev. D* **13**, 3398 (1976).
- [38] M. Z. Hasan and C. L. Kane, *Colloquium: Topological insulators*, *Rev. Mod. Phys.* **82**, 3045 (2010).
- [39] X.-L. Qi and S.-C. Zhang, Topological insulators and superconductors, *Rev. Mod. Phys.* **83**, 1057 (2011).
- [40] C. L. Kane and E. J. Mele, Quantum spin Hall effect in graphene, *Phys. Rev. Lett.* **95**, 226801 (2005).
- [41] B. A. Bernevig, T. L. Hughes, and S.-C. Zhang, Quantum spin Hall effect and topological phase transition in HgTe quantum wells, *Science* **314**, 1757 (2006).
- [42] G. Siroki, P. A. Huidobro, and V. Giannini, Topological photonics: From crystals to particles, *Phys. Rev. B* **96**, 041408(R) (2017).
- [43] See Supplemental Material at <http://link.aps.org/supplemental/10.1103/PhysRevResearch.7.023067> for more details of theoretical analysis, numerical simulations and experimental steps.
- [44] COMSOL Multiphysics@v. 6.0. www.comsol.com. COMSOL AB, Stockholm, Sweden.
- [45] S. Y. Siew, B. Li, F. Gao, H. Y. Zheng, W. Zhang, P. Guo, S. W. Xie, A. Song, B. Dong, L. W. Luo, C. Li, and X. Luo, Review of silicon photonics technology and platform development, *J. Light. Technol.* **39**, 4374 (2021).
- [46] G. E. Jellison and H. H. Burke, The temperature dependence of the refractive index of silicon at elevated temperatures at several laser wavelengths, *J. Appl. Phys.* **60**, 841 (1986).
- [47] M. V. Berry, Quantal phase factors accompanying adiabatic changes, *Proc. R. Soc. London Ser. A* **392**, 45 (1984).
- [48] D. Xiao, M.-C. Chang, and Q. Niu, Berry phase effects on electronic properties. *Rev. Mod. Phys.* **82**, 1959 (2010).

- [49] S. A. Skirlo, L. Lu, and M. Soljačić, Multimode one-way waveguides of large Chern numbers, *Phys. Rev. Lett.* **113**, 113904 (2014).
- [50] W. Tang, M. Wang, S. Ma, C. T. Chan, and S. Zhang, Magnetically controllable multimode interference in topological photonic crystals, *Light Sci. Appl.* **13**, 112 (2024).
- [51] J.-W. Dong, X.-D. Chen, H. Zhu, Y. Wang, and X. Zhang, Valley photonic crystals for control of spin and topology, *Nat. Mater.* **16**, 298 (2017).
- [52] M. J. Ablowitz, J. T. Cole, and S. D. Nixon, Switching via wave interaction in topological photonic lattices, *Opt. Lett.* **49**, 734 (2024).
- [53] H. Kagami, T. Amemiya, S. Okada, N. Nishiyama, and X. Hu, Topological converter for high-efficiency coupling between Si wire waveguide and topological waveguide, *Opt. Express* **28**, 33619 (2020).
- [54] X. Chen, J. Lin, and K. Wang, A review of silicon-based integrated optical switches, *Laser Photonics Rev.* **17**, 2200571 (2023).
- [55] C. He, X. Ni, H. Ge, X.-C. Sun, Y.-B. Chen, M.-H. Lu, X.-P. Liu, and Y.-F. Chen, Acoustic topological insulator and robust one-way sound transport, *Nat. Phys.* **12**, 1124 (2016).
- [56] J. Cha, K. W. Kim, and C. Daraio, Experimental realization of on-chip topological nanoelectromechanical metamaterials, *Nature (London)* **564**, 229 (2018).